Photochemical & Photobiological Sciences

PAPER

Cite this: *Photochem. Photobiol. Sci.*, 2019, **18**, 2259

Synthesis, spectroscopy and QM/MM simulations of a biomimetic ultrafast light-driven molecular motor†‡

Igor Schapiro, §¶[a] Moussa Gueye,¶[a] Marco Paolino, ¶[b] Stefania Fusi, [b] Gabriel Marchand,[a] Stefan Haacke, [a] M. Elena Martin, [c] Mark Huntress,‖[d] Victor P. Vysotskiy,[e] Valera Veryazov, [e] Jérémie Léonard [a] and Massimo Olivucci *[b,d]

Received 14th May 2019,
Accepted 16th July 2019

DOI: 10.1039/c9pp00223e

rsc.li/pps

A molecular motor potentially performing a continuous unidirectional rotation is studied by a multidisciplinary approach including organic synthesis, transient spectroscopy and excited state trajectory calculations. A stereogenic center was introduced in the *N*-alkylated indanylidene–pyrroline Schiff base framework of a previously investigated light-driven molecular switch in order to achieve the unidirectional C=C rotary motion typical of Feringa's motor. Here we report that the specific substitution pattern of the designed chiral molecule must critically determine the unidirectional efficiency of the light-induced rotary motion. More specifically, we find that a stereogenic center containing a methyl group and a hydrogen atom as substituents does not create a differential steric effect large enough to fully direct the motion in either the clockwise or counterclockwise direction especially along the $E \rightarrow Z$ coordinate. However, due to the documented ultrafast character and electronic circular dichroism activity of the investigated system, we find that it provides the basis for development of a novel generation of rotary motors with a biomimetic framework and operating on a picosecond time scale.

Introduction

Rotary molecular motors are molecular devices capable of performing multiple, unidirectional 360° torsional motions as a response to energy inputs.[1] In recent years many efforts have been devoted to the design and synthesis of new motors driven by external stimuli such as a reversible chemical reaction or light irradiation.[2–6] Among these options, light irradiation represents an important renewable external energy source used in so-called rotary light-driven molecular motors (LDMMs) of the Feringa type.[7] In such types of LDMM,[1] a chiral molecule featuring a single exocyclic double bond undergoes a four step sequential process. This process includes a unidirectional (clockwise or counterclockwise) $Z \rightarrow E$ (or $E \rightarrow Z$) double bond photoisomerization, a thermal conformational change, a second unidirectional $E \rightarrow Z$ (or $Z \rightarrow E$) double-bond photoisomerization and a final thermal conformational change resulting in the reconstitution of the initial reactant through a full 360° double bond rotation.

In the past, our group developed a series of ultrafast rotary light-driven molecular switches (LDMSs) based on the *N*-alkyl indanylidene pyrrolinium (NAIP) framework and designed to mimic the photoisomerization of the protonated Schiff base of retinal (rPSB) found in Rhodopsin (Rh): a widely studied vertebrate visual pigment.[8–13] NAIP molecules perform a regioselective subpicosecond double bond photoisomerization similar to that observed for the isomerization of the 11-*cis* double bond of the rPSB chromophore of Rh.[14,15] Furthermore, contrary to other LDMSs, NAIPs have a positive

[a]*Université de Strasbourg, CNRS, UMR 7504, Institut de Physique et Chimie des Matériaux de Strasbourg, 23 du Loess, 67034 Strasbourg, France*
[b]*Dipartimento di Biotecnologia, Chimica e Farmacia (Dipartimento di Eccellenza 2018-2022), Università degli Studi di Siena, via Aldo Moro 2, I-53100 Siena, Italy. E-mail: massimo.olivucci@unisi.it, molivuc@bgsu.edu*
[c]*Area de Química Física, Universidad de Extremadura, Avenida de Elvas sn, E-06071 Badajoz, Spain*
[d]*Chemistry Department, Bowling Green State University, Bowling Green Ohio 43403, USA*
[e]*Division of Theoretical Chemistry, Kemicentrum, Lund University, P.O. Box 124, Lund, SE-221 00, Sweden*

†Dedicated to the memory of Professor Ugo Mazzucato of the University of Perugia, Italy.

‡Electronic supplementary information (ESI) available: Two trajectory movies (echiral.006.md.xyz and zchiral.004.md.xyz). See DOI: 10.1039/c9pp00223e

§Present address: Fritz Haber Center for Molecular Dynamics Research at the Institute of Chemistry, the Hebrew University of Jerusalem, Jerusalem 91904, Israel.
¶These authors have equally contributed to the research.
‖Present address: Patrick Henry Community College in Martinsville, VA 24112, USA.

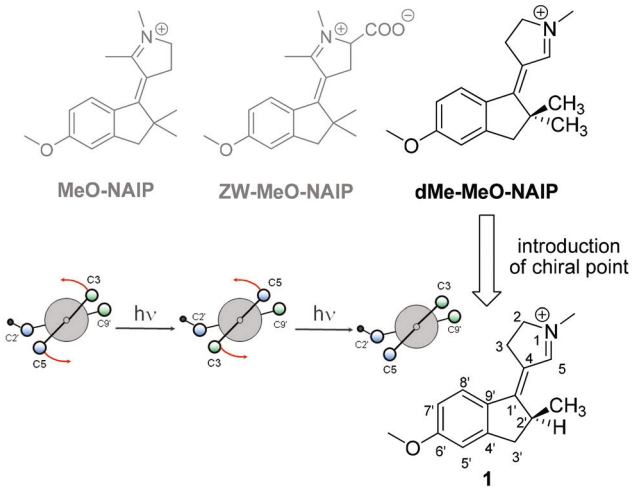

Fig. 1 Structure of previously reported MeO-NAIP and dMe-MeO-NAIP LDMSs and of the new chiral compound **1** together with its Newman projection along the isomerizing double bond representing the desired unidirectional rotation.

charge and, thus, represent alternative charged systems for the development of synthetic single-molecule rotary LDMMs with possible applications in various fields such as nanotechnology, and synthetic biology.[16]

However, a unidirectionally isomerizing NAIP system, which would be required to achieve a Feringa's type LDMM, has not been developed yet although the design of NAIP-like systems has been proposed.[17,18] To this end, we introduce a stereogenic center into a NAIP-based LDMS to achieve the new LDMM **1** (Fig. 1), examine its photoreaction properties using transient absorption (TA) spectroscopy and rationalize the corresponding findings by modeling the excited state dynamics using a small set of nonadiabatic trajectories.

Results and discussion

Design, synthesis and photochemistry

We decided to start from the previously published compound dMe-MeO-NAIP[11,12] (Fig. 1). Contrary to its analogue photoswitch MeO-NAIP,[19] the absence of the methyl group on the pyrrolinium ring of dMe-MeO-NAIP confers a flat geometry to the molecule.[9,12,19] Therefore, using the skeleton of dMe-MeO-NAIP for the introduction of a stereogenic center ensures that the resulting putative out-of-plane deformations are due to such structure modification and not to pre-existing strain effects. The synthetic strategy is to include an asymmetric carbon in the C2′ position. As predicted by the computational investigation of a related, reduced model compound,[20] this is expected to affect the direction of torsional deformation associated to the double bond isomerization without changing the electronic structure of the molecule and in a way similar to Feringa's LDMM.[1]

The retrosynthetic analysis of **1** led us to identify, as convenient starting material, the *N*-Boc pyrrolidinone **2**, easily obtainable from the commercially available pyrrolidin-2-one, and the synthetically available compound **3** (Fig. 2).[21]

The synthesis is described in detail in Scheme 1. The initial aldol condensation reaction of the lithium enolate of compound **2** with the BF_3-activated carbonyl group of the indanone **3**, followed by dehydratation in acid environment, led to the *E* and *Z* forms of the lactam derivative **4**. The latter was protected as *N*-Boc derivative to obtain the diastereoisomers **5***E* and **5***Z*.

5*E*/*Z* was then employed in a one-pot synthesis yielding the corresponding cyclic imines, through the reduction with DIBAL-H, followed by dehydration and cleavage of the protective group using trifluoromethanesulfonic acid to finally obtain the free base NAIP precursor **6***E* (negligible amount of the diastereoisomer 6*Z* was obtained). This compound, then provides the photoswitchable 4-(5-methoxy-2-methyl-2,3-dihydro-1*H*-inden-1-ylidene)-1-methyl-3,4-dihydro-2*H*-pyrrol-1-ium trifluoromethanesulfonate **1***E* after quaternarization of the nitrogen atom with methyl triflate.

In this way, we get the chiral switch **1***E* as a racemic mixture ready for enantiomeric separation. Unfortunately, at this level the separation of the two enantiomers by HPLC equipped with a chiral column failed.

Thus, to obtain the pure enantiomers of compound **1***E* we acted at the level of the intermediate **5** (Scheme 2).

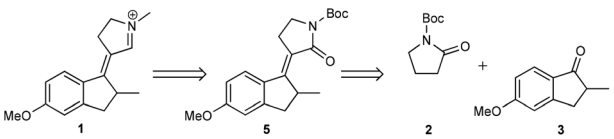

Fig. 2 Retrosynthetic analysis of **1**.

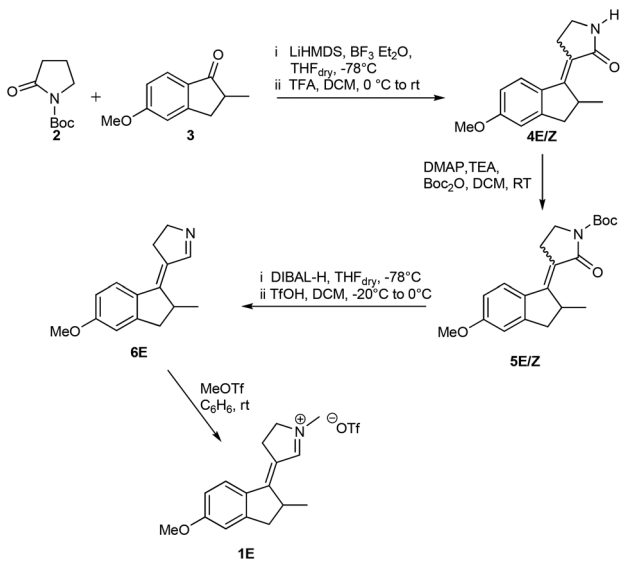

Scheme 1 Synthesis of chiral compound **1**.

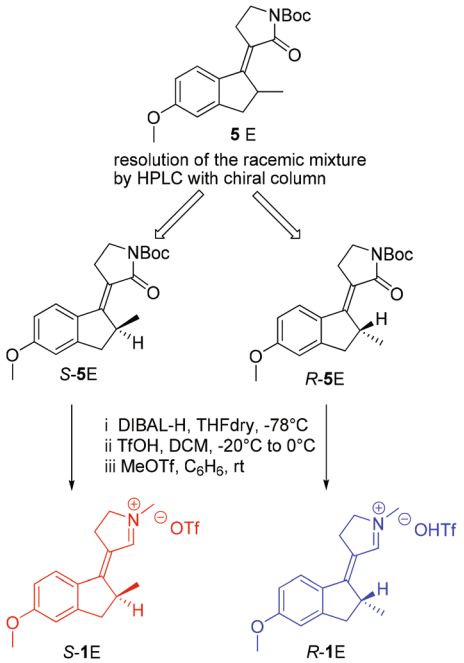

Scheme 2 Synthesis of enantiomerically pure compounds *R*-**1***E* and *S*-**1***E*.

The resolved **5***E* enantiomers were used as starting materials to carry out the synthesis of compound **1** as described above. This set of reactions were consistent with the retention of the configuration of the stereogenic center allowing us to prepare (see Scheme 2) the two enantiomerically pure switches *R*-**1***E* and *S*-**1***E* as confirmed by the circular dichroism spectra reported in Fig. 3b.

The pure geometric isomer **5***E* was obtained by classic flash chromatography and its enantiomeric mixture was resolved by preparative HPLC. Fig. 3a displays the circular dichroism spectra of the *R* and *S* enantiomers of **5***E*.

The UV spectrum in MeOH of **1***E* displays an absorption maximum at 387 nm (Fig. 4). Then, a solution of **1***E*/*Z* (ratio *E*/*Z* = 1/0.05) in $CDCl_3$ was irradiated at room temperature in a NMR pyrex tube at different wavelengths (λ = 348 nm, 387 nm, and 428 nm). The photoisomerization reactions were monitored by ^{1}H NMR until the photostationary states are reached. At this point, the corresponding *E*/*Z* compositions were determined as reported in Table 1.

As shown in the table, distinct compositions were reached upon irradiation at different wavelengths, demonstrating the possibility to modulate the isomeric equilibrium. Moreover, the resulting mixtures were stored at room temperature in the dark for a few days without observing any significant composition change.

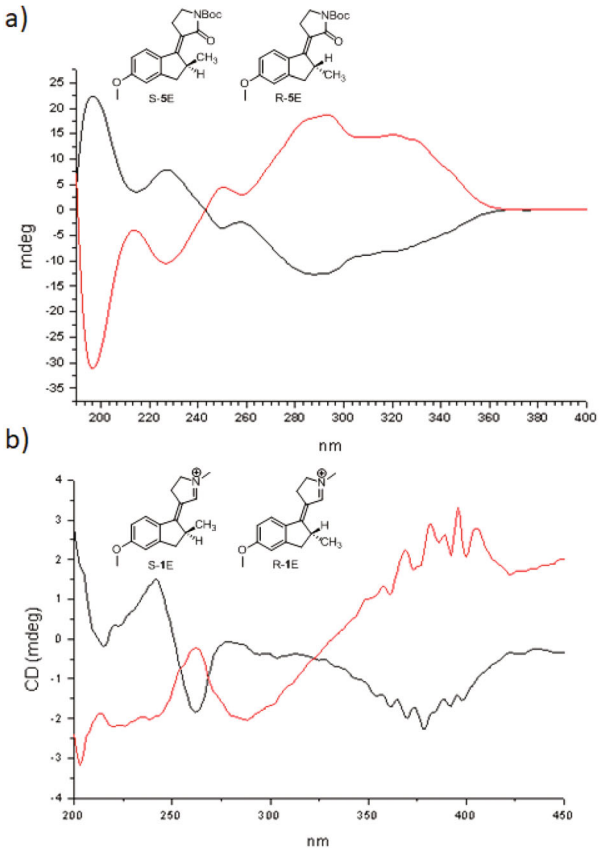

Fig. 3 Qualitative CD spectra of the pure enantiomers of compounds **5***E* (a) and **1***E* (b). The difference in shape, loss of mirror image symmetry and odd features seen in part b are due to instrumental limitations in measuring low intensities.

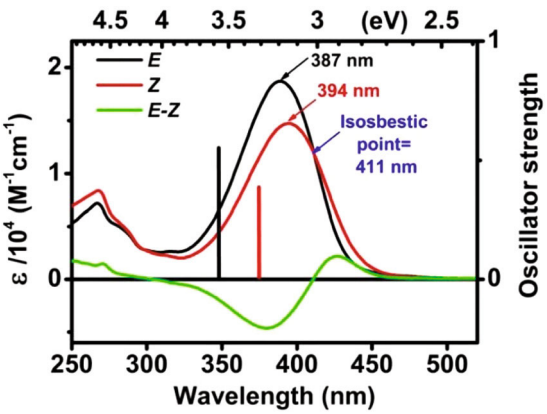

Fig. 4 Steady-state absorption spectra of the pure **1***E* isomer (black) and pure **1***Z* isomer (red) measured in MeOH together with their difference (green). The calculated excitation energies (CASPT2 level of theory) are shown as stick spectra and based on geometries from the ASEP/MD procedure.

Photoisomerization dynamics

Transient absorption (TA) spectroscopy was performed on a racemic mixture of **1** produced as illustrated in Scheme 1, and dissolved in MeOH. The TA data of two samples of **1** at the same total concentration but featuring different *E*/*Z* isomer compositions were recorded after 400 nm excitation. By computing the appropriate linear combination of these two data

Table 1 Photostationary state of compound **1** at different wavelengths

λ (nm)	E	Z
348 (a)	1	0.97
387 (b)	1	1.25
428 (c)	1	0.34

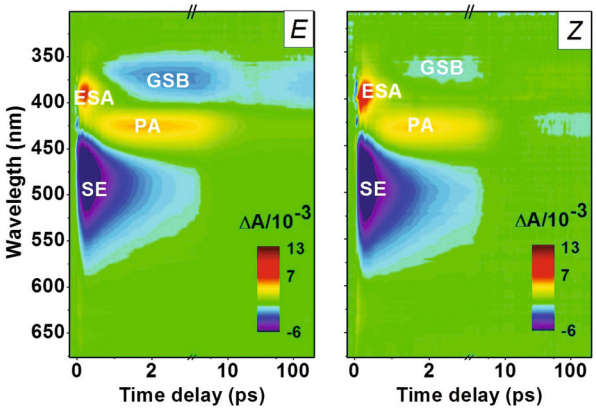

Fig. 5 Pump-induced absorption change ΔA (coded with a false-color scale) as a function of probe wavelength (in nm) and pump–probe time delay (ps) of the pure E (left) and the pure Z (right) isomers of **1** in MeOH.

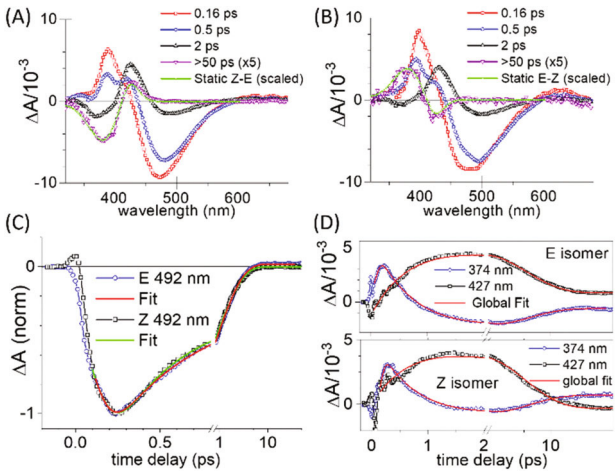

Fig. 6 TA data on the E and Z diastereoisomers of **1** in MeOH. Selection of transient spectra for (A) the pure E and (B) the pure Z compounds. (C) Kinetic traces at 492 nm (SE) for both isomers and their fit. (D) Kinetic traces at 374 nm (ESA and GSB) and 427 nm (PA) and their global fit for the pure E and pure Z isomers.

sets (see Experimental section) we have reconstructed the TA data of the pure diastereoisomers, which are displayed in Fig. 5 in the form of 2D maps. Fig. 6 presents a selection of TA spectra (Fig. 6A and B) and TA decay kinetics (Fig. 6C and D) extracted from these 2D maps.

For both diastereoisomers, we observe at short time delays very similar spectroscopic signatures of the S_1 excited state essentially composed of stimulated emission (SE, negative signal coded in blue in the range of 430–580 nm) and excited state absorption (ESA, positive signal code in red in the range of 370–420 nm). The intense ESA band overlaps with the less intense ground state bleach (GSB, negative signal) which is thus hidden at very short time delays, but is detected as a weak negative signal between 350 and 400 nm at later times (>0.5 to 1 ps), when the ESA signature has decayed. Concomitant with the ESA and SE decays, the spectroscopic signature of the vibrationally hot photoproduct absorptions (PA, positive signal) emerges after ~0.5 ps and further rises in the range of 410–450 nm. A priori, since the isomerization quantum yields are <1, both vibrationally hot E and Z diastereoisomers are produced upon decay to S_0. Fig. 4 shows that both have very similar absorption spectra at ambient temperature, and it is known that vibrationally hot molecules have an absorption spectrum which broadens, in particular towards long wavelengths.[22,23] Hence we interpret this early PA as the signature of the vibrationally hot, S_0 absorption of – *a priori* – both isomers. Both TA datasets look very similar until vibrational cooling has occurred. Only then, *i.e.* after ~30 ps, a quasi-static, vibrationally-relaxed spectrum is observed up to 100 ps for both molecules (hardly seen in Fig. 5, but evident in Fig. 6).

Fig. 6A and B display a selection of transient spectra for both isomers. At early times (160 fs), the S_1 signatures are the ESA, maximum at 390 nm for E and 400 nm for Z, and the SE, maximum at 470 nm (E) or 480 nm (Z). A weak red ESA is also seen at λ > 600 nm, in particular for Z (Fig. 6B). On the 0.5 ps time scale, the ESA and SE signatures decay and the vibrationally hot PA band rises with a maximum at ~425 nm (E) and ~430 nm (Z). After 2 ps, the GSB clearly appears (negative signal around 370 nm for both isomers) due to the significant decay of the overlapping ESA. At the same time delay, SE has also significantly decayed but it is still detectable. After complete decay from S_1, further vibrational relaxation occurs in the vibrationally hot ground state on the several ps time scale until a quasistationary spectrum is observed (>50 ps). The latter overlaps with the difference between E and Z static absorption spectra, thus evidencing the formation of Z when exciting E and *vice versa*. From the amplitudes of these quasistationary differential spectra, and by comparison with other NAIP compounds, we determine that the E-to-Z and Z-to-E photoisomerization quantum yields are 24% and 20%, respectively.[24]

The photoreaction kinetics are essentially identical for both isomers. In particular, Fig. 6C compares the 492 nm traces indicative of the SE kinetics of both isomers. Interestingly, the SE signal rises beyond 0.1 or 0.15 ps with a somewhat reduced slope until it reaches its maximum at ~250 fs. This rise time is not limited by the experimental resolution and is indicative of excited state vibrational relaxation away from the Franck Condon region on the same time scale. We note that the early, weak, red ESA decays on this time scale also. Then the SE decay is well fitted by a biexponential function with time scales τ_1 = 250 to 310 fs and τ_2 = 1.3 ps for both isomers. The time constants and their relative weights are given in Table 2 for each isomer.

Table 2 Fitting results

	E	*E*	*Z*	*Z*
λ (nm)	492 (SE)	374 (ESA) and 427 (PA)	492 (SE)	374 (ESA) and 427 (PA)
Rise (ps)	0.25	0.25[a]	0.25	0.25[a]
τ_1 (ps)	0.31 (40%)	0.7[b]	0.25 (50%)	0.7[b]
τ_2 (ps)	1.3 (60%)	4.8[b]	1.3 (50%)	4.8[b]

[a] At 374 nm only. [b] No relative weight is given for these two time constants since they correspond to different processes, namely S_1 lifetime (τ_1) and vibrational relaxation time scale in S_0 (τ_2).

Unlike the SE kinetic trace which reveals only the S_1 decay kinetics, the ESA is observed in the same wavelength range as GSB and PA. Hence the corresponding kinetic trace reveals time constants pertaining to both excited and ground state dynamics as we will discuss now. As illustrated in Fig. 6D for each isomer, the decay of the ESA (at 374 nm) is synchronous to the rise of the PA (at 427 nm). For both isomers, a rise time is also clearly resolved in the ESA signal (374 nm) which becomes maximal after ~250(±30) fs. Then, the 374 nm and 427 nm traces are fitted simultaneously with a biexponential function while seeking identical time constants in both traces (global fitting). The same analysis is repeated independently on both isomers and yields exactly the same time constants as seen in Table 2, supporting the conclusion that both isomers have the same photoreaction kinetics. The first time constant τ_1 = 0.7 ps is common to the decay of the ESA and the rise of the PA. It is thus attributed to the excited state population decay and photoproduct formation. This time constant should be considered as a combination of the two SE decay time constants hence as an average excited state lifetime. The second time constant τ_2 = 4.8 ps is common to further relaxation of the PA signal (observed at 427 nm after the PA rise) and of the GSB (observed at 372 nm after the ESA decay). Hence, the 4.8 ps time can be attributed to ground state spectral relaxation induced by vibrational relaxation.

Finally, we observe that the traces at 427 nm display oscillations at early times (but beyond the spoiling solvent contributions). These are rapidly damped and have a ~150 fs oscillation period, corresponding to a 220 cm^{-1} mode already reported for the achiral dME-MeO-NAIP.[9]

Due to its planarity the overall photoreaction dynamics of compound **1** is actually very similar to that of the non-chiral dMe-MeO-NAIP, that is in contrast to the vibrationally coherent scenario reported for the parent MeO-NAIP (which carries a methyl group on C5 and is non-planar).[9]

Simulations

The Averaged Solvent Electrostatic Potential/Molecular Dynamics (ASEP/MD)[25,26] protocol was used to calculate the excitation energies. First, the geometry of MeOH in solution was determined in an iterative procedure. Both diastereoisomers have a nearly planar C1′═C4 bond. However, the *E* isomer is slightly more planar, with the dihedral angles C9′–C1′–C4–C5 and C2′–C1′–C4–C3 deviating by 1.8 and 1.5 degrees, respectively, from the plane. In comparison, the *Z* isomer is distorted by 6.0 and 0.4 degrees from planarity for C9′–C1′–C4–C5 and C2′–C1′–C4–C3.

The excitation energies were calculated using the CASPT2/CASSCF(10,10)/6-31G* level of theory for the MeOH. The results are provided in Fig. 4 along with the corresponding measured quantities. The computed absorption maxima and relative intensities display the same qualitative order for the *E* and *Z* isomers as their experimental counterparts. However, the excitation energies are systematically overestimated. The shift between the *E* and *Z* isomer in MeOH solution is in qualitative agreement with the experiment due to error cancellation.

In order to study the mechanism of the excited state evolution of the system and complement the experimental data presented in the previous section, we have computed four non-adiabatic QM/MM trajectories for each diastereoisomer. We found that for both *R*-**1***E* and *R*-**1***Z*, only 3 out of 4 trajectories successfully isomerized. While these results indicate that the isomerization cannot, as expected, be fully efficient, the trajectory analysis below focuses on the mechanistic details of the atomic displacements (*i.e.* on the directionality of the torsional deformation of the rotor with respect to the stator) characterizing the isomerization motion. More specifically, we are interested to see if the chiral switch shows a preferential clockwise or counterclockwise direction of C═C torsional deformation to be associated to the presence of the stereogenic center.

Representative trajectories for *R*-**1***E* and *R*-**1***Z* are illustrated in Fig. 7 (an unreactive trajectory) and 8 (a reactive trajectory) respectively. In Fig. 7 the trajectory starts from the FC point on the second excited state which initially displays the highest oscillator strength and therefore is the spectroscopic, bright state. However, only few fs into the simulations there is a transition between S_2 and S_1. After such transition, S_1 becomes the bright state as it correlates with the one observed spectroscopically. However, the initial CASSCF state order is inverted at the more accurate CASPT2 level of theory (see Experimental section) which indicates that S_1 is always the bright state. Thus, the initial order is a consequence of the CASSCF level of approximation which, however, only impacts few fs of the initial trajectory computation.

When following the evolution along the S_1 excited state (see top panel in Fig. 7) one can see that at *ca.* 300 fs the S_1 and S_2 energy gap starts to increase while the S_1 potential energy profile decreases. Subsequently, a conical intersection between S_1 and S_0 is reached at 461 fs. The geometrical evolution associated to these changes can be described in terms of sequential bond stretching and torsion. First, the C4═C1′ exocyclic double bond undergoes an immediate elongation of about 0.2 Å and essentially becomes a single bond. This allows a torsional deformation around the same bond, as shown by the C9′–C1′═C4–C5 and C2′–C1′–C4–C3 dihedral angles which increases up to *ca.* 90 degrees when the conical intersection region is entered. This deformation constitutes a dominant

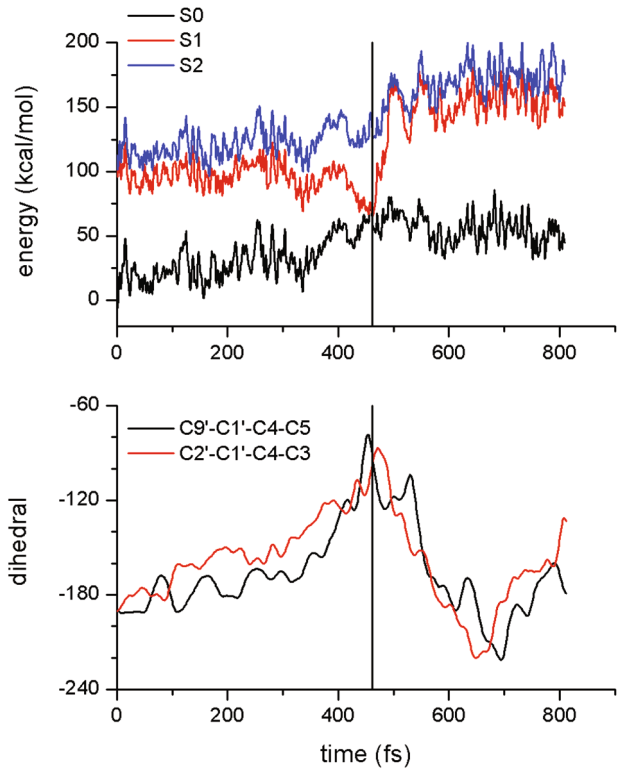

Fig. 7 An unreactive QM/MM trajectory of compound *R*-**1***E* (see ESI movie echiral.006.md.xyz‡). The Franck–Condon excitation takes place at t = 0 fs. The computed nonadiabatic transition is indicated by a vertical lines at 461 fs. Top: Evolution of the energies for the lowest three electronic states at the CASSCF/Amber level of theory. Bottom: Evolution of the dihedral angle of the exocyclic double bond defined in two different ways.

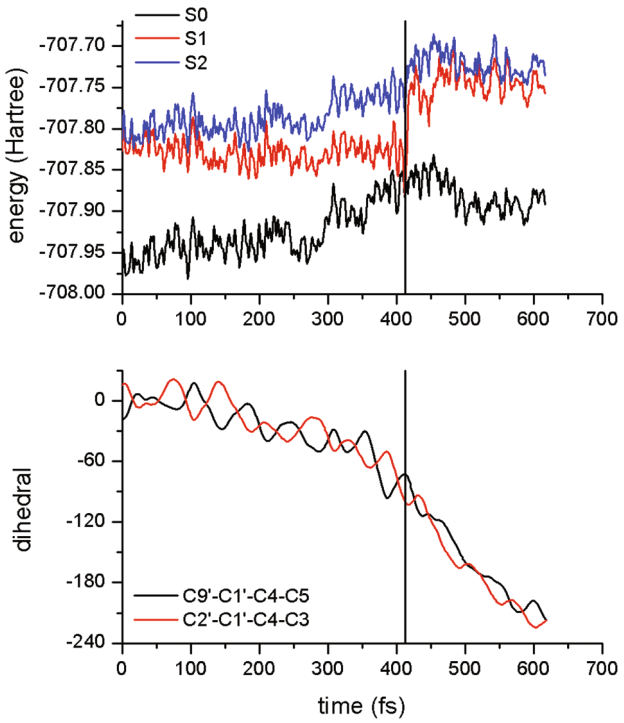

Fig. 8 A reactive QM/MM trajectory of compound *R*-**1***Z* (see ESI movie zchiral.004.md.xyz‡). The Franck–Condon excitation takes place at t = 0 fs. The computed nonadiabatic transition is indicated by a vertical line at 413 fs. Top: Evolution of the energies for the lowest three electronic states at the CASSCF//Amber level of theory. Bottom: Evolution of the dihedral angle of the exocyclic double bond defined in two different ways.

contribution to the S_1 relaxation coordinate. It is coupled with the ring inversion motion of the indanylidene and pyrrolinium rings, as evidenced by the changes of the C1′=C4–C3–C2 and the C4–C3–C2–N dihedral angles. The ring inversions contribute to the torsion around C4=C1′ while minimizing the required space and conserving the position of the center of mass of both rings during the early stage of the isomerization dynamics. An analogous evolution was observed during the isomerization of MeO-NAIP[14] and ZW-NAIP (see Fig. 1).[27]

In the case of the successfully isomerizing *R*-**1***Z* trajectory displayed in Fig. 8 we observe that a rotation of more than 180° is predicted to occur in a unique, ultrafast photochemical step. This is in contrast to the mechanism of the Feringa's molecular motor where a 180° rotation requires, in addition to the initial photochemical step, a rate-limiting, thermally activated ground state structural rearrangement, before a second photon may trigger the next half turn in the same rotation direction.[7,28] In our molecular motor, the probability of achieving a full 360° rotation upon sequential absorption of two photons resulting in two ultrafast half turns is controlled by the probability that both diastereoisomers rotate in the same direction. In a previous theoretical investigation of a related but simplified compound,[20] we demonstrated that the presence of a single stereogenic center as in compound **1** is indeed sufficient to increase the probability of a unidirectiotnal rotation up to 76% for each isomer. Thus, a stereogenic center may induce a net directionality in the two-step 360° rotation. With compound **1**, we note that, in all *R*-**1***Z* trajectories, the rotor shows a preference for twisting in the clockwise direction (C9′–C1′=C4–C5 and C2′–C1′=C4–C3 dihedrals decreasing in value), as expected when considering the steric interaction of the methylene group at C3 with the methyl substituent at C2′. However, for *R*-**1***E* in 3 trajectories out of four the rotor is twisting in the opposite counterclockwise direction (C9′–C1′=C4–C5 and C2′–C1′=C4–C3 dihedrals increasing in value), in spite of the steric interaction between the vinyl H at C5 and the same methyl substituent at C2′ (Table 3).

After inspecting Table 3, we also conclude, and this is confirmed by inspection of other *R*-**1***E* trajectories, that the pretwist is not a safe criterium to predict the directionality of the rotation when its magnitude is small (few degrees) and, therefore, the system is relatively planar. In this condition, a London attractive force between the small H atom at position C5 and the methyl substituent at position C2′ may bias the counterclockwise directionality.

Although the present number of only four trajectories is not statistically relevant, *e.g.* as compared to ensembles of 200 tra-

Table 3 Non-adiabatic molecular dynamics trajectories for the *R*-1*E* and *R*-1*Z* isomers. The initial values (degrees) of the dihedrals C9′–C1′–C4–C5; C2′–C1′–C4–C3 are reported along with the values at the surface hop (*i.e.* near the CI). R and NR indicate reactive and non-reactive trajectories respectively. CW and CCW indicate clockwise and counterclockwise isomerization motion respectively

	R-1*Z*				*R*-1*E*			
Traj.	001	002	004	007	001	003	006	007
Initial value	+15; −7	−4; 0	−18; +15	−33; −3	+177; −173	−179; +171	+172; +170	+175; +176
Value at CI	−82; −81	−78; −94	−73; −100	−99; −102	−112; −69	+91; +88	−90; −98	−127; −62
React.	NR	R	R	R	R	R	NR	R
Direct.	CW	CW	CW	CW	CCW	CW	CCW	CCW

jectories in our previous investigation of the reduced model,[20] this behavior of the *R*-1*E* isomer indicates that the designed chiral switch may not yield a fully effective unidirectional rotation consistently with the result reported for the corresponding model compound.[20] In other words, our study only provides information on the existence of certain directionality preference rather than on their actual statistical impact on the population behavior.

Conclusion

In the present work we have shown that it is possible to prepare and spectroscopically characterize a chiral NAIP-based photochemical switch which could, in principle, behave as an ultrafast LDMM. We have demonstrated that this compound undergoes ultrafast *E* to *Z* and *Z* to *E* photoisomerizations, with no rate-limiting intermediate step, and with relatively good quantum yields as compared to the <2% photoisomerization quantum yields reported for the Feringa-type molecular rotary motors.[1] However, the analysis of a few trajectories indicates that its unidirectional efficiency may be low or reduced due to the lack of full unidirectionality especially in the *E* to *Z* photochemical step. More specifically, the two diastereoisomers may have opposite (clockwise *versus* counterclockwise) predominant rotation direction, thus impairing the directionality of the rotary motion. A qualitative structural analysis indicates that this behavior is possibly due to the differences in the interaction of the substituents in positions C5 and C3 with the methyl group in position C2′. Indeed, due to the asymmetric steric interaction between the methylene group at C3 with the methyl substituent at C2′ the *Z* isomer would probably achieve a fully clockwise unidirectional motion. In contrast, in the *E* isomer operates a reduced steric repulsion between the vinyl H at C5 and the same methyl substituent at C2′ which may be possibly accompanied by a weak attractive force. Accordingly, the *E* diastereoisomer would be directed in both the clockwise and counterclockwise rotation direction also consistently with its higher planarity. However, since only a few trajectories have been computed, this is a mechanistic rather than a statistical observation.

In spite of the suspected inefficiency, both the TA spectroscopic studies and trajectory calculations show that the photoisomerizations of the two isomers would conserve the ultrafast dynamics already documented for the previously reported achiral analogue LDMS dMe-MeO-NAIP. In one case (see Fig. 8) we also predicted that the double bond isomerization could overcome the half-rotation threshold, pointing to a small or absent barrier controlling the thermal conformational change usually following the photoisomerization in a Feringa's type switch[1] and indicating the possibility of achieving higher rotary speed and directionalities as also pursued by others in different systems.[29] The above results are encouraging as the design and preparation of an efficient LDMM would mainly require the synthesis of a homologue of **1** displaying at C2′ two suitably designed alkyl substituents (*e.g.* a methyl and isopropyl) rather than a methyl substituent and a hydrogen atom. Furthermore, when preparing a chiral molecular switch which could be investigated by time-resolved electronic CD experiments, it is necessary to design a chiral system with a higher CD intensity. These two complementary research targets are currently carried on in our labs.

Experimental section

Synthesis

All chemicals used were of reagent grade. Yields refer to purified products and are not optimized. Merck silica gel 60 (230–400 mesh) was used for column chromatography. Merck TLC plates and silica gel 60 F254 were used for TLC. ^{1}H NMR spectra were recorded at 400 MHz (Bruker DRX-400 AVANCE spectrometer) in the indicated solvents (TMS as internal standard): the values of the chemical shifts are expressed in ppm and the coupling constants (J) in Hz. An Agilent 1100 LC/MSD operating with an electrospray source was used in mass spectrometry experiments. Photochemical experiments were carried out with a photoirradiation system equipped with a 900 W Xenon source and a high radiance monochromator. The enantiomeric separation of compound **5***E* was performed by HPLC (Agilent) equipped with a Chiralpak AD–H (5 μm 46 × 250 mm) using heptanes/ethanol (8 : 2) as eluent (flow rate of 1.0 mL min^{-1}). CD spectra were recorded in methanol using a Jasco J-815 CD spectrometer.

3-(5-Methoxy-2-methyl-2,3-dihydro-1*H*-inden-1-ylidene)pyrrolidin-2-one (4). Compound **4** was prepared modifying a previously reported procedure.[30] To a solution of *N*-Boc-2-pyrrolidinone (**2**) (0.17 g, 0.94 mmol) dissolved in anhydrous THF

(5 mL), a 1 M solution of lithium hexamethyldisilazide (LiHMDS) in anhydrous THF (1.08 mL, 1.08 mmol) was added at −78 °C under a nitrogen atmosphere. After 1 h, a solution of compound **3**[21] (0.26 g, 1.49 mmol) and $BF_3{\cdot}Et_2O$ (1.49 mmol, 188 μL) in anhydrous THF (3 mL) was added dropwise. The reaction mixture was stirred at −78 °C for 3 h. Then, NH_4Cl (s.s.) was added, and the crude was extracted with CH_2Cl_2. The combined organic layers were dried over Na_2SO_4 and concentrated under reduced pressure. The oily residue was dissolved in CH_2Cl_2 (10 mL), and trifluoroacetic acid (0.6 mL) was added. The resulting reaction mixture was stirred at room temperature for 30 min. Then, $NaHCO_3$ (s.s.) was added and the crude was extracted with CH_2Cl_2. The residue was purified by flash chromatography using ethyl acetate/petroleum ether (1 : 1) as eluent to obtain compound **4** as white solid (*E*/*Z* ratio = 8 : 2, 0.11 g, yield 48%). ^{1}H-NMR (400 MHz, $CDCl_3$): 1.10 (d, *J* = 7.2, 3H minor isomer), 1.18 (d, *J* = 7.2, 3H major isomer), 2.50 (d, *J* = 16.0, 1H minor isomer), 2.57 (d, *J* = 16.0, 1H major isomer), 2.86–3.26 (m, major and minor isomer), 3.40–3.61 (m, 2H, minor isomer), 3.81 (s, 3H minor isomer), 3.83 (s, 3H major isomer), 4.21 (m, 1H major isomer), 5.61 (br s, 1H major isomer), 5.95 (br s, 1H minor isomer), 6.65 (s, 1H minor isomer), 6.79 (d, *J* = 8.8, 1H minor isomer), 6.83 (d, *J* = 8.6, 1H major isomer), 6.88 (s, 1H major isomer), 7.41 (d, *J* = 8.6, 1H major isomer), 9.04 (d, *J* = 8.8, 1H minor isomer). *m*/*z* (ESI): 266 ($M + Na^+$).

tert*-Butyl 3-(5-methoxy-2-methyl-2,3-dihydro-1*H*-inden-1-ylidene)-2-oxopyrrolidine-1-carboxylate (5).** A mixture of compound **4** (0.10 g, 0.41 mmol), di-*tert*-butyl dicarbonate (0.18 g, 0.82 mmol), *N*,*N*-dimethylpyridin-4-amine (DMPA, 0.010 g, 0.082 mmol) in dichloromethane (15 mL) was stirred at room temperature under argon atmosphere for 18 h. Then, the reaction mixture was washed with water and the organic layer was dried over sodium sulphate and concentred under reduced pressure. The residue was purified by flash chromatography using petroleum ether–ethyl acetate (8 : 2) as eluent to obtain compound **5** (*E*/*Z* ratio = 8 : 2, 0.13 g, 92%) as pale yellow solid. A racemic mixture of pure *E* isomer was obtain by flash chromatography using gradient elution from petroleum ether to a mixture of petroleum ether–ethyl acetate (8 : 2). **5E* ^{1}H-NMR (400 MHz, $CDCl_3$): 1.13 (d, *J* = 7.2 Hz, 3H), 1.50 (s, 9H), 2.52 (d, *J* = 16.4, 1H), 2.78–3.01 (m, 2H), 3.10 (dd, *J* = 16.4, 7.2, 1H), 3.62–3.73 (m, 1H), 3.76–3.86 (m, 4H), 4.11–4.20 (m, 1H), 6.78 (d, *J* = 8.8, 1H), 6.83 (s, 1H), 7.36 (d, *J* = 8.8, 1H). ^{13}C-NMR (100 MHz, $CDCl_3$) 22.23, 23.80, 27.98, 37.24, 39.59, 43.04, 55.14, 82.06, 110.28, 113.44, 117.68, 127.14, 132.07, 151.09, 151.25, 158.70, 161.39, 167.52. **5***Z* ^{1}H-NMR (400 MHz, $CDCl_3$): 1.06 (d, *J* = 6.8, 3H), 1.52 (s, 9H), 2.48 (d, *J* = 16.4, 1H), 2.71–2.88 (m, 2H), 3.00–3.06 (m, 1H), 3.16 (dd, *J* = 16.4, 1H), 3.70–3.81 (m, 5H), 6.71–6.77 (m, 2H), 9.08 (d, *J* = 8.8). ^{13}C-NMR (100 MHz, $CDCl_3$) 19.91, 24.33, 28.10, 38.90, 41.09, 43.27, 55.27, 82.13, 109.58, 112.11, 112.78, 119.10, 129.89, 131.80, 150.71, 151.12, 158.83, 161.51, 167.03. *m*/*z* (ESI): 456 ($M + Na^+$).

4-(5-Methoxy-2-methyl-2,3-dihydro-1*H*-inden-1-ylidene)-3,4-dihydro-2*H*-pyrrole (6). Diisobutylaluminum hydride solution in hexanes (0.53 mmol, 0.53 mL) was added dropwise to a cooled (−78 °C) solution of the *E*/*Z* mixture of compound **5** (0.12 g, 0.35 mmol) in dry THF (5 mL) under nitrogen atmosphere. After being stirred at −78 °C for 1 h, the reaction mixture was diluted with H_2O (5 mL) and 1 N HCl (5 mL) and extracted with CH_2Cl_2. The organic layer was dried over Na_2SO_4 and concentred under reduced pressure. The residue was dissolved in CH_2Cl_2 (5 mL) and cooled at −20 °C followed by treatment with trifluoromethanesulfonicacid (3.50 mmol, 305 μL). The resulting solution was stirred for 1 h at 0 °C, then, $NaHCO_3$ (s.s.) was added, and the mixture was extracted with CH_2Cl_2. The organic layer was dried over Na_2SO_4 and concentrated under vacuum to give a residue which was purified by flash chromatography using Et_2O on silica gel conditioned with TEA to obtain compound **6** ((ratio *E*/*Z* = 1/0.05) 66 mg, 68%) as yellow oil. ^{1}H-NMR (400 MHz, $CDCl_3$): 1.15 (d, *J* = 6.8, 3H, minor isomer), 1.19 (d, *J* = 7.2, 3H, major isomer), 2.53 (d, *J* = 15.2, 1H minor isomer), 2.57 (d, *J* = 16.0, 1H, major isomer), 2.67–2.81 (m, minor and major isomer), 2.80–3.52 (m, minor and major isomer), 3.71–3.90 (m, minor and major isomer), 4.00–4.21(m, minor and major isomer), 6.73–6.87 (m, minor and major isomer), 7.38 (d, *J* = 8.4, 1H, major isomer), 7.45 (d, *J* = 8.4, 1H, minor isomer), 8.08 (s, 1H, major isomer), 9.17 (s, 1H, minor isomer). *m*/*z* (ESI): 227 ($M + H^+$).

4-(5-Methoxy-2-methyl-2,3-dihydro-1*H*-inden-1-ylidene)-1-methyl-3,4-dihydro-2*H*-pyrrolium (1). Methyl trifluoromethanesulfonate (0.22 mmol, 26 μL) was added to a solution of compound **6***E* (0.050 g, 0.22 mmol) in anhydrous benzene (5 mL). The reaction mixture was stirred for 1 h at room temperature under nitrogen atmosphere, then the solvent was removed under reduced pressure obtaining quantitatively the compound **1***E* as orange oil. ^{1}H-NMR (400 MHz, $CDCl_3$) (*E* isomer): 1.28 (d, *J* = 7.2, 3H), 2.66 (d, *J* = 16.8, 1H), 3.20–3.37 (m, 3H), 3.69 (s, 3H), 3.74–3.82 (m, 1H), 3.86 (s, 3H), 4.18–4.30 (m, 2H), 6.87–6.92 (m, 2H), 7.46 (d, *J* = 9.2, 1H), 8.97 (s, 1H). ^{13}C-NMR (100 MHz, $CDCl_3$): 25.06, 27.36, 39.14, 39.80, 39.89, 55.68, 58.20, 110.37, 115.52, 123.53, 128.31, 130.10, 154.91, 168.54, 169.26. *m*/*z* (ESI): 242 (M^+). After photochemical reaction ^{1}H-NMR data of the geometric isomer **1***Z* are derived. ^{1}H-NMR (400 MHz, $CDCl_3$) (*Z* isomer): 1.16 (d, *J* = 6.8, 3H), 2.60 (d, *J* = 16.8, 1H), 3.09–3.21 (m, 3H), 3.72 (s, 3H), 3.74–3.82 (m, 1H), 3.83 (s, 3H), 4.09–4.18 (m, 2H), 6.80 (s, 1H), 6.92–6.95 (m, 1H), 7.99 (d, *J* = 8.8, 1H), 9.25 (s, 1H).

Spectroscopy and photochemistry

Transient Absorption Spectroscopy (TAS) is used to study the photoisomerization dynamics in methanol of a racemate of the chiral photoswitch **1**. The experimental set-up was described in details in ref. 13. In short, a 400 nm pump pulse is generated by SHG of the 40 fs, 800 nm fundamental beam of a 5 kHz amplified Ti:Sa laser system. The probe is a white light supercontinuum generated at 800 nm in a CaF2 crystal. Both pump and probe beams are focused into a 0.2 mm-thick quartz flow cell containing **1** dissolved in MeOH. The sample is circulated using a peristaltic pump so as to refresh the

sample between two excitation laser shots. The relative polarizations of pump and probe beam are set to magic angle (54.7°). The intensity of the pump beam is kept in the linear regime of excitation, so as to promote the molecule to its first excited electronic state S_1 only.

^{1}H-NMR spectroscopy allows us to determine the relative *E* and *Z* content of the solution used in the TAS experiment. In the dark at room temperature, the composition of the "dark state" (DS) solution is 95% *E* and 5% *Z*. We split this sample in two and irradiate one of the two at 333 nm until a photostationary state (PSS) is obtained. The PSS solution has a composition of 38% *E* and 62% *Z*, and no thermally-activated back isomerization is observed at room temperature after switching off the 333 nm light. We then perform TAS successively on both DS and PSS samples, under identical experimental conditions. Knowing the *E* : *Z* composition of both sample, allows us to compute the appropriate linear combination of both TAS data sets (see ref. 24 for details) and retrieve the TAS data of pure *E* and pure *Z* compounds as shown in Fig. 5. Hence both *E* to *Z* and *Z* to *E* photoreactions are investigated separately and compared.

All TAS data presented here are post-processed in order to compensate for the group velocity dispersion in the probe beam so as to define accurately the time zero at all wavelengths. Quantitative data analysis is performed by fitting the data with model functions. At very early times, the non-linear interaction of pump and probe beams in the solvent generates a time- and wavelength–dependent signal. The latter is recorded separately in the pure solvent, but cannot be accurately corrected for, and kinetics traces are spoiled at very early times by this "solvent" signal. Therefore the fits only start after ~0.1 or 0.15 ps. Despite this difficulty, at various wavelengths, the signal is observed to rise on a time scale slower than the experimental time resolution, and a Gaussian shape (more precisely the error function "erf") is used to fit this rise. Then further time evolution is fitted by sums of exponential decaying curves (see *e.g.* ref. 13, 14 and 16).

Simulations

The explicitly solvated chiral switch model was constructed by preparing a rectangular box of methanol molecules where each atom of the switch was at least 10 Å away from the boundary (Fig. 9). In order to compensate the positive charge of the switch, one chloride ion was added to the solvent box. The average ground-state configuration of the methanol molecules (that is, the solvent) was determined according to the following procedure. The solvent was relaxed by 1000 conjugate-gradient minimization steps using periodic boundary conditions while keeping the chromophore (*i.e.*, the solute) fixed in its gas-phase configuration. The parametrization was based on the general force field in Amber, while charges were determined using a restrained electrostatic potential (RESP) procedure[31,32] at the HF/6-31G* level of theory. This starting structure was then used to sample the initial conditions for excited state molecular dynamics simulations and averaged solvent electrostatic potential/molecular dynamics (ASEP/MD)[33] calculations of the excitation energies.

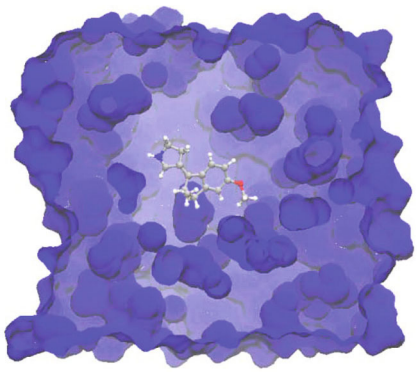

Fig. 9 Chiral molecule **1** in the methanol solvent.

The initial conditions for the excited state molecular dynamics simulations were generated according to the following protocol. First, a fully classical trajectory of 0.5 ns length was generated. Then snapshots of the last, equilibrated part were taken every 10 ps. In order to relax the switch we first run a ground state hybrid quantum mechanics/molecular mechanics (QM/MM) trajectory of 0.5 ps starting from every snapshot. This time is sufficient because the switch is relatively small compared to the solvent. The final structures were then used to run excited state QM/MM trajectory calculations.

The QM/MM partitioning defined the molecular switch as part of the quantum mechanics (QM) subsystem and the remaining methanol as part of the molecular mechanics (MM) subsystem. The CASSCF method was employed to describe the QM part, while the Amber parameter were describing the methanol molecules. We use electrostatic embedding using the ESPF model.[34] The active space comprised the full conjugated π-system, namely 10 electrons in 10 π-type orbitals. For excited state trajectory we have averaged the lowest three roots. For quantitative calculation of excitation energies we accounted for dynamic electron correlation by CASPT2 calculation. The QM/MM calculations were carried out using the programs Molcas 7.8[35] interfaced with TINKER5.[36,37] The Velocity Verlet algorithm was used for numerical integration of Newton's equations of motions with a time step of 1 fs. In order to detect a non-adiabatic transition, we have used a deterministic surface hopping algorithm.[38]

The ASEP/MD simulations were carried out based on the well-established protocol.[31] Briefly, ASEP/MD method is a sequential QM/MM mechanics (QM/MM) that makes use of the mean field approximation (MFA).[33,39] In this approximation, instead of considering specific solvent configurations, the perturbation enters into the solute molecular Hamiltonian in an averaged way. Consequently, ASEP/MD through the MFA permits to reduce the number of quantum calculation from several thousands, as usual in QM/MM[40] methods, to only a few, and the highest levels of theory available at present can be employed. We have employed the MP2 method to optimize the geometry in the ground state because it is known to provide accurate structural parameters.

Author contributions

I. S., M. P., J. L. and M. O. wrote the manuscript; I. S., G. M., M. E. M., M. H., V. P. V. and V. V. executed the computational part of the research; M. P. and S. F. executed the organic synthesis of the investigated compounds; M. G., S. H. and J. L. performed the spectroscopic measurements.

Conflicts of interest

There are no conflicts to declare.

Acknowledgements

M. P., S. F. and M. O. acknowledge an MIUR (Ministero dell'Istruzione, dell'Università e della Ricerca) grant "Dipartimento di Eccellenza 2018–2022". M. O. and M. P. are grateful for a MIUR-PRIN 2015 grant (2015RNWJAM_005). We acknowledge support from the Region Alsace (Contrat doctoral, No. 607-12-C31) and from the French Agence Nationale de la Recherche *via* grant No. ANR-11-JS04-010-01 "IPQCS" and the program "Investissement d'Avenir": ANR-10-IDEX-0002-02, ANR-11-LABX-0058_NIE, ANR-10-LABX-0026_CSC.

Notes and references

1 D. Roke, S. J. Wezenberg and B. L. Feringa, *Proc. Natl. Acad. Sci. U. S. A.*, 2018, **115**, 9423–9431.
2 R. D. Astumian, *Chem. Sci.*, 2017, **8**, 840–845.
3 S. Erbas-Cakmak, S. D. P. Fielden, U. Karaca, D. A. Leigh, C. T. McTernan, D. J. Tetlow and M. R. Wilson, *Science*, 2017, **358**, 340–343.
4 B. S. L. Collins, J. C. M. Kistemaker, E. Otten and B. L. Feringa, *Nat. Chem.*, 2016, **8**, 860.
5 C. R. Hall, J. Conyard, I. A. Heisler, G. Jones, J. Frost, W. R. Browne, B. L. Feringa and S. R. Meech, *J. Am. Chem. Soc.*, 2017, **139**, 7408–7414.
6 J. C. M. Kistemaker, P. Štacko, J. Visser and B. L. Feringa, *Nat. Chem.*, 2015, **7**, 890.
7 N. Koumura, R. W. J. Zijlstra, R. A. van Delden, N. Harada and B. L. Feringa, *Nature*, 1999, **401**, 152–155.
8 C. Schnedermann, X. Yang, M. Liebel, K. M. Spillane, J. Lugtenburg, I. Fernández, A. Valentini, I. Schapiro, M. Olivucci, P. Kukura and R. A. Mathies, *Nat. Chem.*, 2018, **10**, 449–455.
9 M. Gueye, M. Manathunga, D. Agathangelou, Y. Orozco, M. Paolino, S. Fusi, S. Haacke, M. Olivucci and J. Léonard, *Nat. Commun.*, 2018, **9**, 313.
10 I. Schapiro, S. Fusi, M. Olivucci, T. Andruniów, S. Sasidharanpillai and G. R. Loppnow, *J. Phys. Chem. B*, 2014, **118**, 12243–12250.
11 R. Rossi Paccani, D. Donati, S. Fusi, L. Latterini, G. Farina, V. Zanirato and M. Olivucci, *J. Org. Chem.*, 2012, **77**, 1738–1748.
12 A. D. Dunkelberger, R. D. Kieda, J. Y. Shin, R. Rossi Paccani, S. Fusi, M. Olivucci and F. Fleming Crim, *J. Phys. Chem. A*, 2012, **116**, 3527–3533.
13 J. Briand, O. Braem, J. Rehault, J. Léonard, A. Cannizzo, M. Chergui, V. Zanirato, M. Olivucci, J. Helbing and S. Haacke, *Phys. Chem. Chem. Phys.*, 2010, **12**, 3178–3187.
14 J. Léonard, I. Schapiro, J. Briand, S. Fusi, R. R. Paccani, M. Olivucci and S. Haacke, *Chem. – Eur. J.*, 2012, **18**, 15296–15304.
15 K. Pagano, M. Paolino, S. Fusi, V. Zanirato, C. Trapella, G. Giuliani, A. Cappelli, S. Zanzoni, H. Molinari, L. Ragona and M. Olivucci, *J. Phys. Chem. Lett.*, 2019, **10**, 2235–2243.
16 S. Gozem, F. Melaccio, H. L. Luk, S. Rinaldi and M. Olivucci, *Chem. Soc. Rev.*, 2014, **43**, 4019–4036.
17 A. Nikiforov, J. A. Gamez, W. Thiel and M. Filatov, *J. Phys. Chem. Lett.*, 2016, **7**, 105–110.
18 J. Wang and B. Durbeej, *ChemistryOpen*, 2018, **7**, 583–589.
19 V. Zanirato, G. P. Pollini, C. De Risi, F. Valente, A. Melloni, S. Fusi, J. Barbetti and M. Olivucci, *Tetrahedron*, 2007, **63**, 4975–4982.
20 G. Marchand, J. Eng, I. Schapiro, A. Valentini, L. M. Frutos, E. Pieri, M. Olivucci, J. Léonard and E. Gindensperger, *J. Phys. Chem. Lett.*, 2015, **6**, 599–604.
21 E. Alcalde, N. Mesquida, S. López-Pérez, J. Frigola, R. Mercè, J. Holenz, M. Pujol and E. Hernández, *Bioorg. Med. Chem.*, 2009, **17**, 7387–7397.
22 W. Wild, A. Seilmeier, N. H. Gottfried and W. Kaiser, *Chem. Phys. Lett.*, 1985, **119**, 259–263.
23 T. Robl and A. Seilmeier, *Chem. Phys. Lett.*, 1988, **147**, 544–550.
24 M. Gueye, M. Paolino, E. Gindensperger, S. Haacke, M. Olivucci and J. Léonard, *Faraday Discuss.*, DOI: 10.1039/C9FD00062C.
25 A. Muñoz Losa, I. F. Galván, M. E. Martín and M. A. Aguilar, *J. Phys. Chem. B*, 2006, **110**, 18064–18071.
26 M. E. Martín, A. M. Losa, I. F. Galván and M. A. Aguilar, *J. Mol. Struct.: THEOCHEM*, 2006, **775**, 81–86.
27 A. Melloni, R. Rossi Paccani, D. Donati, V. Zanirato, A. Sinicropi, M. L. Parisi, E. Martin, M. Ryazantsev, W. J. Ding, L. M. Frutos, R. Basosi, S. Fusi, L. Latterini, N. Ferré and M. Olivucci, *J. Am. Chem. Soc.*, 2010, **132**, 9310–9319.
28 M. Klok, N. Boyle, M. T. Pryce, A. Meetsma, W. R. Browne and B. L. Feringa, *J. Am. Chem. Soc.*, 2008, **130**, 10484–10485.
29 A. Gerwien, P. Mayer and H. Dube, *J. Am. Chem. Soc.*, 2018, **140**, 16442–16445.
30 M. Paolino, M. Gueye, E. Pieri, M. Manathunga, S. Fusi, A. Cappelli, L. Latterini, D. Pannacci, M. Filatov, J. Léonard and M. Olivucci, *J. Am. Chem. Soc.*, 2016, **138**, 9807–9825.
31 C. I. Bayly, P. Cieplak, W. Cornell and P. A. Kollman, *J. Phys. Chem.*, 1993, **97**, 10269–10280.
32 W. D. Cornell, P. Cieplak, C. I. Bayly, I. R. Gould, K. M. Merz, D. M. Ferguson, D. C. Spellmeyer, T. Fox, J. W. Caldwell and P. A. Kollman, *J. Am. Chem. Soc.*, 1995, **117**, 5179–5197.

33 I. F. Galván, M. L. Sánchez, M. E. Martín, F. J. O. del Valle and M. A. Aguilar, *Comput. Phys. Commun.*, 2003, **155**, 244–259.
34 N. Ferré and J. G. Ángyán, *Chem. Phys. Lett.*, 2002, **356**, 331–339.
35 F. Aquilante, L. De Vico, N. Ferré, G. Ghigo, P. Å. Malmqvist, P. Neogrády, T. B. Pedersen, M. PitoNák, M. Reiher, B. O. Roos, L. Serrano, M. Urban, V. Veryazov and R. Lindh, *J. Comput. Chem.*, 2010, **31**, 224–247.
36 J. W. Ponder and F. M. Richards, *J. Comput. Chem.*, 1987, **8**, 1016–1024.
37 F. Melaccio, M. Olivucci, R. Lindh and N. Ferré, *Int. J. Quantum Chem.*, 2011, **111**, 3339–3346.
38 M. Manathunga, *et al.*, *J. Chem. Theory Comput.*, 2016, **12**, 839–850.
39 J. G. Ángyán, *J. Math. Chem.*, 1992, **10**, 93–137.
40 A. Warshel and M. Levitt, *J. Mol. Biol.*, 1976, **103**, 227–249.